Evaluation of Haney–Type Surface Thermal Boundary Conditions Using a Coupled Atmosphere and Ocean Model

Peter C. Chu

Department of Oceanography, Naval Postgraduate School, Monterey, CA 93943, USA

Chen Yuchun (陈玉春) and Lu Shihua (吕世华)

Cold and Arid Regions Environmental and Engineering Research Institute Chinese Academy of Sciences, Lanzhou, 730000

ABSTRACT

A coupled atmosphere–ocean model developed at the Institute for Space Studies at NASA Goddard Space Flight Center (Russell et al., 1995) was used to verify the validity of Haney–type surface thermal boundary condition, which linearly connects net downward surface heat flux Q to air / sea temperature difference ΔT by a relaxation coefficient κ. The model was initiated from the National Centers for Environmental Prediction (NCEP) atmospheric observations for 1 December 1977, and from the National Ocean Data Center (NODC) global climatological mean December temperature and salinity fields at $1° \times 1°$ resolution. The time step is 7.5 minutes. We integrated the model for 450 days and obtained a complete model–generated global data set of daily mean downward net surface flux Q, surface air temperature T_A, and sea surface temperature T_O. Then, we calculated the cross–correlation coefficients (CCC) between Q and ΔT. The ensemble mean CCC fields show (a) no correlation between Q and ΔT in the equatorial regions, and (b) evident correlation (CCC $\geqslant 0.7$) between Q and ΔT in the middle and high latitudes. Additionally, we did the variance analysis and found that when $\kappa = 120$ W m^{-2}K^{-1}, the two standard deviations, σ_Q and $\sigma_{\kappa\Delta T}$, are quite close in the middle and high latitudes. These results agree quite well with a previous research (Chu et al., 1998) on analyzing the NCEP re–analyzed surface data, except that a smaller value of κ (80 W m^{-2}K^{-1}) was found in the previous study.

Key words: Air–sea coupled system, Ocean surface fluxes, Surface thermal boundary condition

1. Introduction

The ocean model is thermally driven by the net downward flux of heat across the ocean surface, Q, which is the sum of the downward flux of solar radiation, R_S, minus the net upward flux of longwave (or "back" radiation), R_b, sensible heat Q_H, and latent heat Q_E,

$$Q = R_S - (R_b + Q_H + Q_E) . \tag{1}$$

Under the assumption that the ocean is in contact with an atmospheric equilibrium state, Haney (1971) obtained a very simple heat flux formulation,

$$Q = \kappa(T_A^* - T_O) \tag{2}$$

where T_A^* is the apparent atmospheric equilibrium temperature, T_O the sea surface

Report Documentation Page

Public reporting burden for the collection of information is estimated to average 1 hour per response, including the time for reviewing instructions, searching existing data sources, gathering and maintaining the data needed, and completing and reviewing the collection of information. Send comments regarding this burden estimate or any other aspect of this collection of information, including suggestions for reducing this burden, to Washington Headquarters Services, Directorate for Information Operations and Reports, 1215 Jefferson Davis Highway, Suite 1204, Arlington VA 22202-4302. Respondents should be aware that notwithstanding any other provision of law, no person shall be subject to a penalty for failing to comply with a collection of information if it does not display a currently valid OMB control number.

1. REPORT DATE **MAY 2001**	2. REPORT TYPE	3. DATES COVERED **00-00-2001 to 00-00-2001**
4. TITLE AND SUBTITLE **Evaluation of Haney-Type Surface Thermal Boundary Conditions Using a Coupled Atmosphere and Ocean Model**		5a. CONTRACT NUMBER
		5b. GRANT NUMBER
		5c. PROGRAM ELEMENT NUMBER
6. AUTHOR(S)		5d. PROJECT NUMBER
		5e. TASK NUMBER
		5f. WORK UNIT NUMBER
7. PERFORMING ORGANIZATION NAME(S) AND ADDRESS(ES) **Naval Postgraduate School ,Department of Oceanography,Monterey,CA,93943**		8. PERFORMING ORGANIZATION REPORT NUMBER
9. SPONSORING/MONITORING AGENCY NAME(S) AND ADDRESS(ES)		10. SPONSOR/MONITOR'S ACRONYM(S)
		11. SPONSOR/MONITOR'S REPORT NUMBER(S)

12. DISTRIBUTION/AVAILABILITY STATEMENT **Approved for public release; distribution unlimited**

13. SUPPLEMENTARY NOTES

14. ABSTRACT

15. SUBJECT TERMS

16. SECURITY CLASSIFICATION OF:			17. LIMITATION OF ABSTRACT **Same as Report (SAR)**	18. NUMBER OF PAGES **21**	19a. NAME OF RESPONSIBLE PERSON
a. REPORT **unclassified**	b. ABSTRACT **unclassified**	c. THIS PAGE **unclassified**			

temperature (SST), and κ is a relaxation coefficient. In spite of its temporal variation, the parameter is usually taken as positive values between 10 to 50 W $m^{-2}K^{-1}$ by various authors (e.g., Marotzke and Stone, 1995; Cai and Chu, 1996). Here T_A^* should be computed from surface heat fluxes and their dependence on temperature, as done by Han (1984) and Oberhuber (1988). Despite Haney's emphasis on that Q is proportional to $T_A^* - T_O$, many subsequent investigators have replaced T_A^* by T_A. Here, T_A is the surface air temperature (SAT). Thus, we call

$$Q = \kappa\Delta T, \qquad \Delta T = T_A - T_O \tag{3}$$

the Haney–type surface boundary condition. Another trend is to separate the solar radiation from the net downward flux (e.g., Blumberg and Mellor, 1987)

$$Q = R_S + \tilde{Q} , \qquad \tilde{Q} \equiv -(R_b + Q_H + Q_E) \tag{4}$$

and to replace Q by $\tilde{Q}$ in the Haney–type surface boundary condition

$$\tilde{Q} = \kappa\Delta T . \tag{5}$$

We call Q the net downward heat flux with solar radiation, and $\tilde{Q}$ the downward heat flux without solar radiation.

Chu et al. (1998) used the global reanalyzed data of Q, surface air temperature T_A, and sea surface temperature T_O from the National Centers for Environmental Prediction (NCEP) from 1 October 1994 to 31 December 1995 to verify the validity of Haney–type surface thermal boundary conditions. They found that the Haney–type surface thermal condition (2) represents the net heat flux quite well for the middle and high latitudes, but very poor in the equatorial regions. Is the result universal or model–dependent? We should use a different type model to verify. Since NCEP constantly has available observational data assimilation, we chose a coupled air–ocean model without data assimilation in this study to see if the previous result (Chu et al., 1998) still holds.

2. A coupled atmospheric–ocean model

2.1 *Model description*

A coupled atmosphere–ocean model (Russell et al., 1995) developed at the NASA Goddard Institute for Space Studies (GISS) was used for this study. The atmospheric model is similar to that of Hansen et al. (1983) except that the atmospheric dynamic equations for mass and momentum are solved using C grid scheme and the advection of potential enthalpy and water vapor uses the linear upstream scheme (Russell and Lerner, 1981). The global ocean model conserves mass, allows for divergent flow, has a free surface and uses the linear upstream scheme for the advection of potential enthalpy and salt. Both models run at $4^\circ \times 5^\circ$ resolution, with 9 vertical layers for the atmosphere and 13 layers for the ocean. Twelve straits are included, allowing for subgrid–scale water flow. Runoff from land is routed into approximate ocean basins. Atmospheric and oceanic surface fluxes of water, heat (excluding solar radiation), and momentum are of opposite sign and are applied synchronously. Flux adjustments are not used. Except for partial strength alternating binomial filters (Shapiro, 1970), which are applied to the momentum components in the atmosphere and oceans, there is no explicit horizontal diffusion. For more information about this coupled model, readers

are referred to Russell et al. (1995). The GISS coupled model was initiated from the NCEP atmospheric observations for 1 December 1977, and from the National Ocean Data Center (NODC) global climatological mean December temperature and salinity fields with $1° \times 1°$ resolution. The time step is 7.5 minutes, and the model was integrated for 450 days. Our purpose here is to build up a dynamically and thermodynamically consistent data set of global surface fluxes R_S, R_b, Q_H, Q_E, and temperatures T_O, T_A, rather than to study physical processes. Thus, a 450-day time integration will provide sufficient data to fulfill this task. However, we should bear in mind that the model surface conditions must change from year to year so that the results in this study may be modified quantitatively.
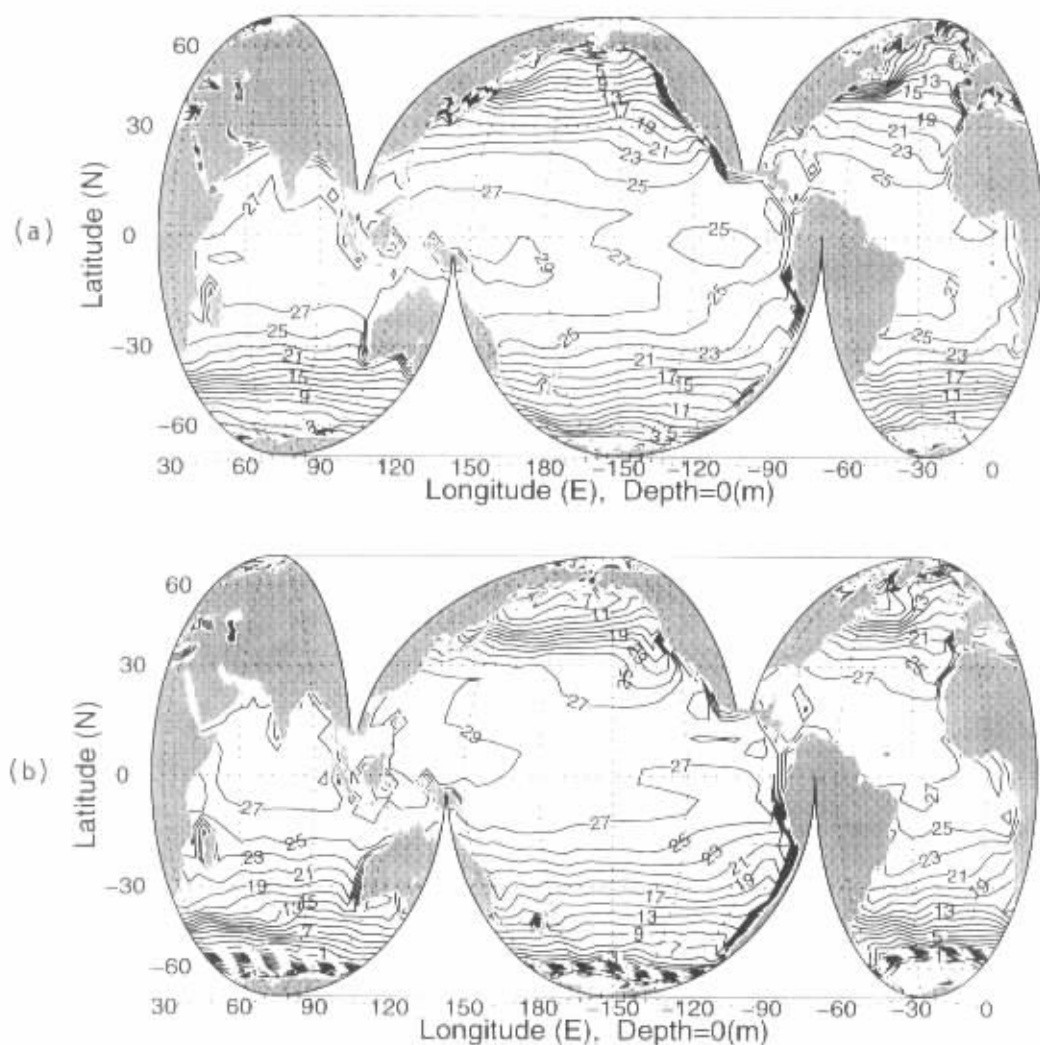

Fig. 1. Monthly mean sea surface temperature (°C) simulated by the GISS Coupled Model: (a) January 1978, and (b) July 1978.

2.2 *Model output*

We choose model generated global surface fluxes R_S, R_b, Q_H, Q_E, and temperatures T_O, T_A data on $4° \times 5°$ grid for this study. Since Haney–type surface thermal boundary conditions are commonly used for ocean modeling on a seasonal time scale or longer, we first computed daily means of these variables to filter out high frequency variability and to obtain a data set of global $Q(x,y,d), \tilde{Q}(x,y,d), T_A(x,y,d), T_O(x,y,d)$ for each day, d, from 1 February 1978 to 5 May 1979.

2.2.1 *Sea surface temperature*

The GISS coupled model simulates a number of interesting sea surface temperature (SST) patterns, indicative of the interaction between ocean and atmosphere (Fig. 1). Western boundary currents such as the Gulf Stream, Kuroshio, Brazil, and Agulhas currents off the eastern shores of North America, Japan, South America, and Southern Africa, respectively appears as meandering bands of warm waters moving poleward into the ocean interior. Large scale, seasonal variation is also simulated. During January (Fig. 1a) the Southern Hemisphere is warm while the cooler temperatures are located in the northern temperate zone. The converse is true in July (Fig. 1b) where we see the other phase of the seasonal cycle. Upwelling and advection leads to large asymmetries in the subtropical thermal structure. The simulated SST fields show the complex connections of the California Current with the equatorial current system, South Pacific eastern boundary current and Peru current.

Furthermore, the model simulates the asymmetric distribution of warm–cool waters in the equatorial regions. We see that the warm water is not only within ocean basins, but also globally with the large warm pool in the western Pacific, Indonesia, and eastern Indian Ocean. The cool water is located in the eastern Pacific. This leads to asymmetric along–equatorial atmospheric circulation – the Walker Cells.

2.2.2 *Surface air temperature*

The GISS coupled model simulates realistic surface air temperature (SAT) variabilities. On monthly fields, a general parallelism exists between SAT and SST (Fig. 2). Large scale, seasonal variation in SAT is also simulated. During January (Fig. 2a) the Southern Hemisphere is warm while the cooler temperatures are located in the northern temperate zone. The converse is true in July (Fig. 2b) where we see the other phase of the seasonal cycle. Large scale zonal asymmetries were also simulated. SAT is low over the upwelling regions, such as California coast. Furthermore, the model simulates the asymmetric distribution of warm–cool SAT in the equatorial regions. We see that the SAT is warmer over the western Pacific warm pool and SAT is cool over the eastern Pacific.

2.2.3 *Ocean–atmosphere heat exchange*

The GISS coupled model simulates realistic variabilities of heat budget at the air–ocean interface, including radiation, sensible heat flux, and latent heat flux.

Short–wave radiation

The amount of solar radiation actually incident on the ocean surface depends on the time of year, the time of day, the latitude, and the atmospheric absorption and scattering (especially by clouds.) Solar radiation is either absorbed by the sea or reflected from its surface. The
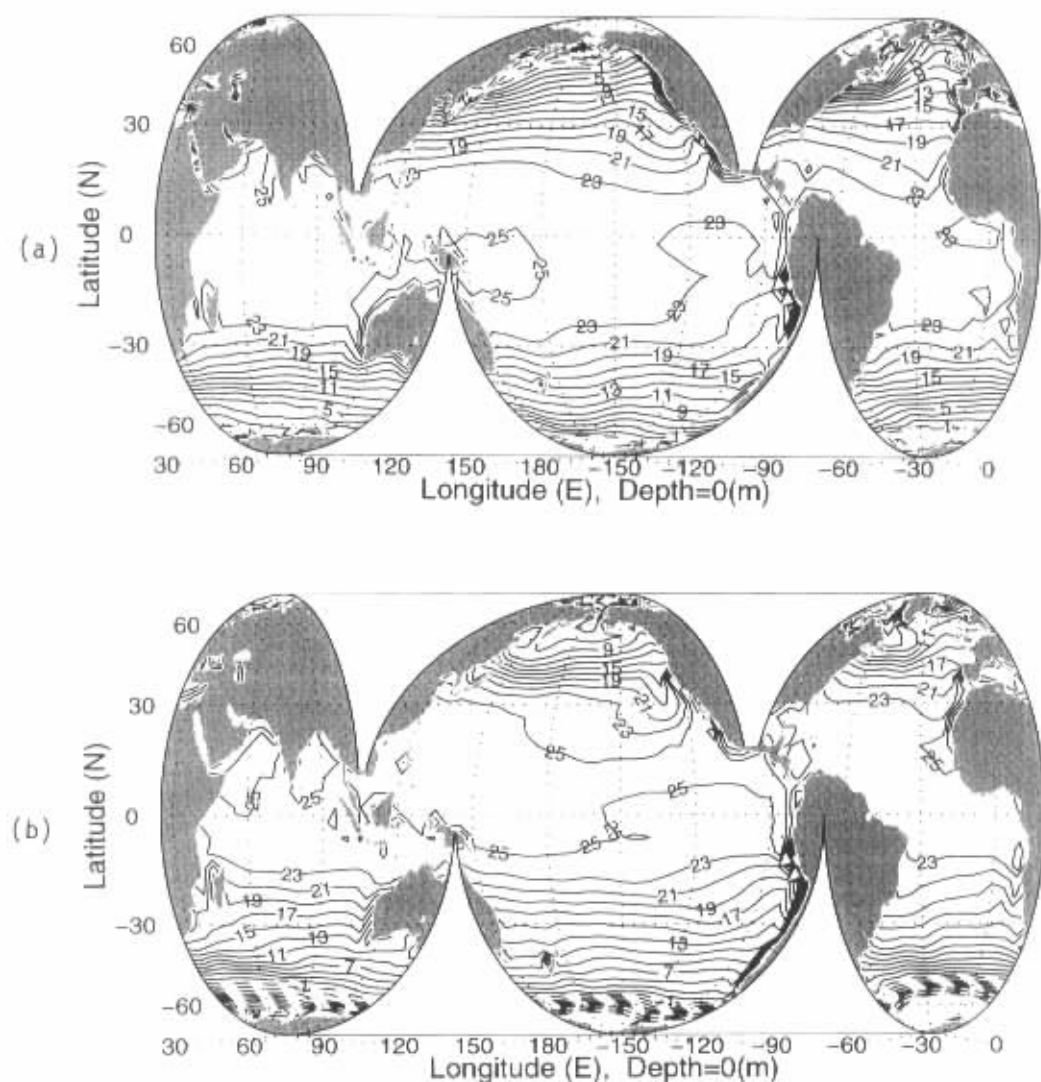
Fig. 2. Monthly mean surface air temperature (°C) simulated by the GISS Coupled Model: (a) January 1978, and (b) July 1978.

degree of reflection (or called the ocean albedo) used by the GISS coupled model is primary a function of solar zenith angle (θ) and surface wind speed (V_s):

$$\alpha_w = 0.012 + 0.0421x^2 + 0.1283x^3 - 0.04x^4 + \frac{3.12x^5}{5.68 + V_s} + \frac{0.074x^6}{1 + 3V_s}$$

where $x = 1 - \cos^{-1}\theta$. This parameterization is based on calculations of Fresnel reflection from the ocean surface as a function of V_s as specified by Cox and Munk (1956). Figure 3 shows the GISS model simulated seasonal variation of the net downward solar radiation over the global ocean surface (R_s). In January (July), the Southern (Northern) Hemisphere ocean surface receives more solar energy than the other hemisphere. For example, an area enclosed
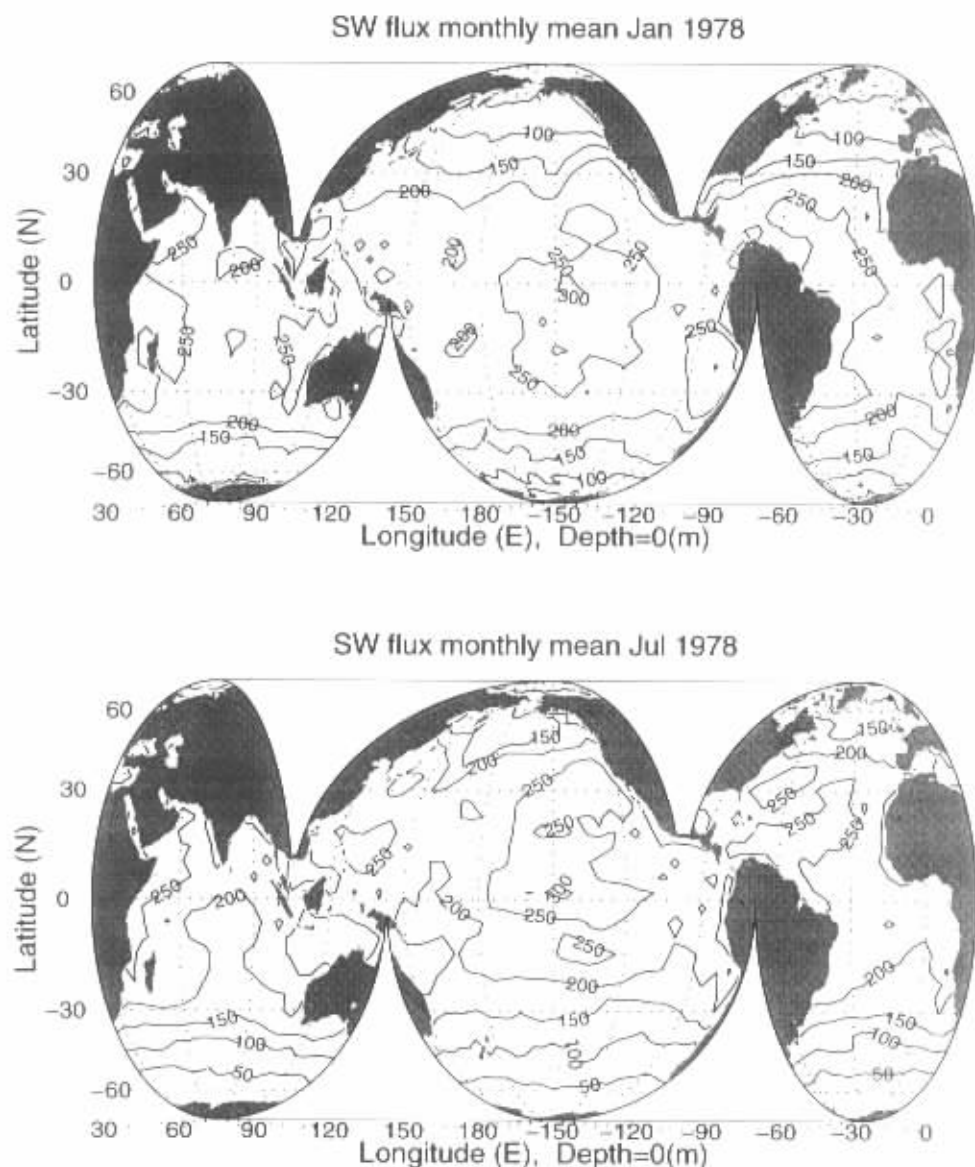
SW flux monthly mean Jan 1978

SW flux monthly mean Jul 1978

Fig. 3. Monthly mean surface net downward solar radiation (W / m²) simulated by the GISS Coupled Model: (a) January 1978, and (b) July 1978.

by the 250 W / m² contour in the central Pacific, shifted toward the Southern (Northern) Hemisphere in January (July) 1978.

Long—wave radiation

Besides absorbing and reflecting solar radiation, the ocean surface also emits radiation of a wavelength appropriate to its temperature and absorbs long—wave radiation transmitted downward from clouds and the atmosphere. Figures 4a and 4b show the GISS coupled model
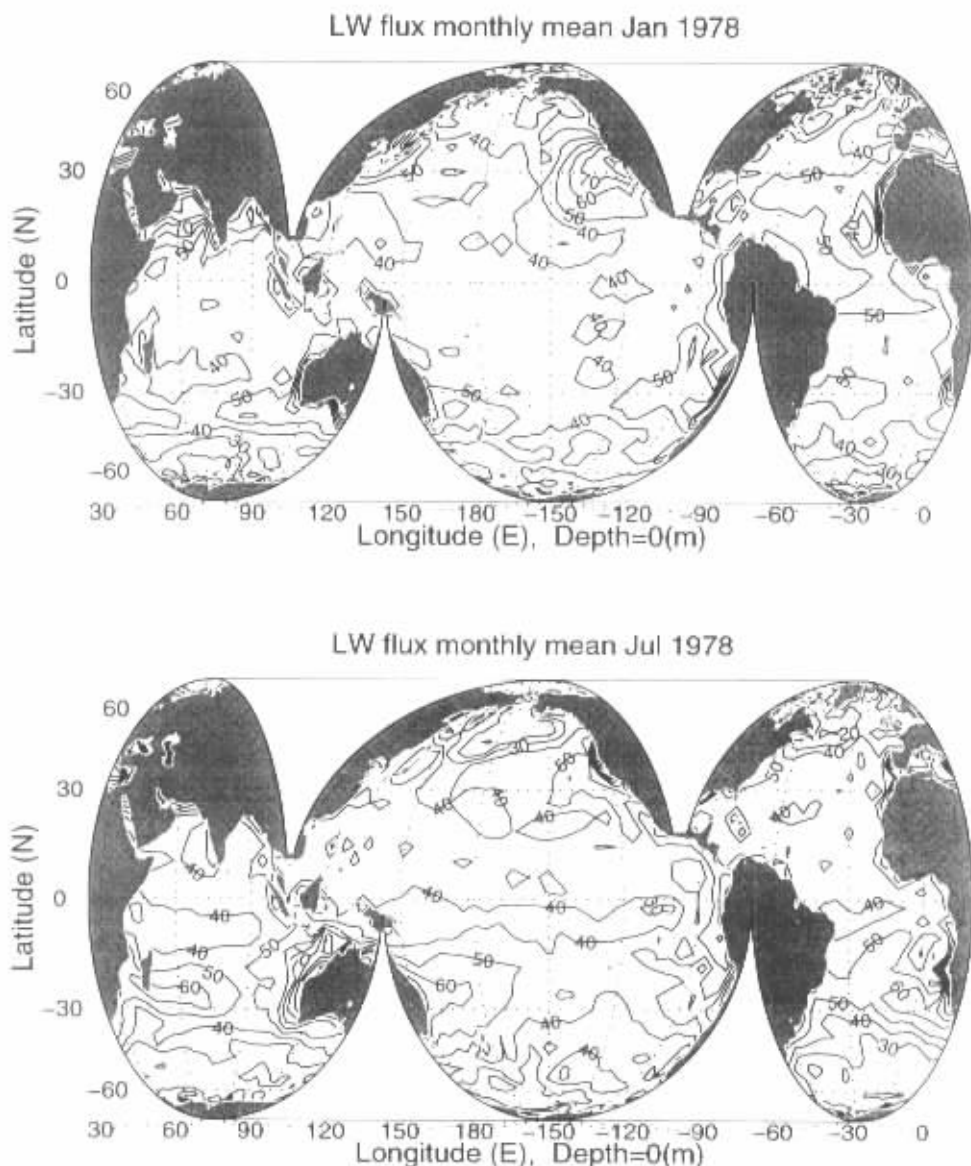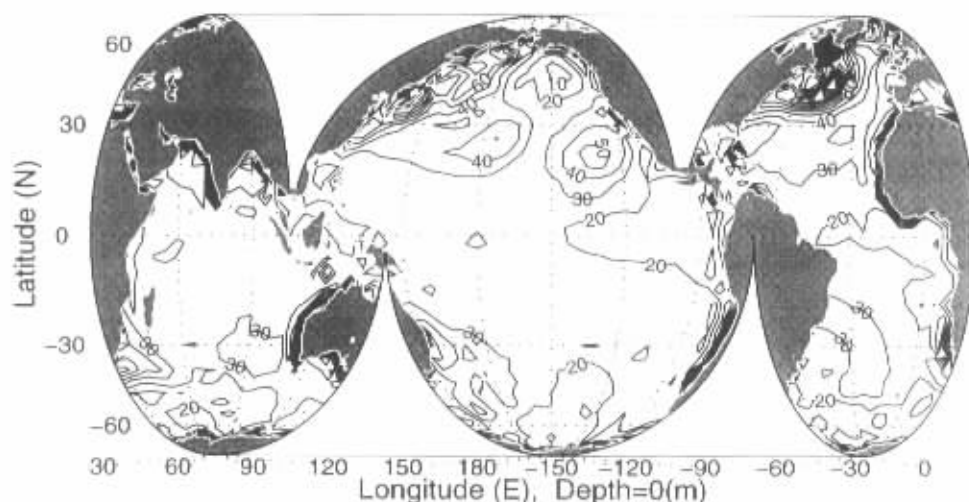
LW flux monthly mean Jan 1978

LW flux monthly mean Jul 1978

Fig. 4. Monthly mean surface net upward long–wave radiation (W / m^2) simulated by the GISS Coupled Model: (a) January 1978, and (b) July 1978.

output of mean January and July (1978) net upward long–wave radiative flux at the ocean surface (R_b), respectively. The magnitude of R_b is much smaller than the magnitude of R_s, which makes the radiation balance of the ocean surface is everywhere positive. This agrees quite well with earlier studies (e.g., Budyko, 1956).

Sensible heat flux

Figures 5a and 5b show the GISS coupled model output of mean January and July

SH flux monthly mean Jan 1978
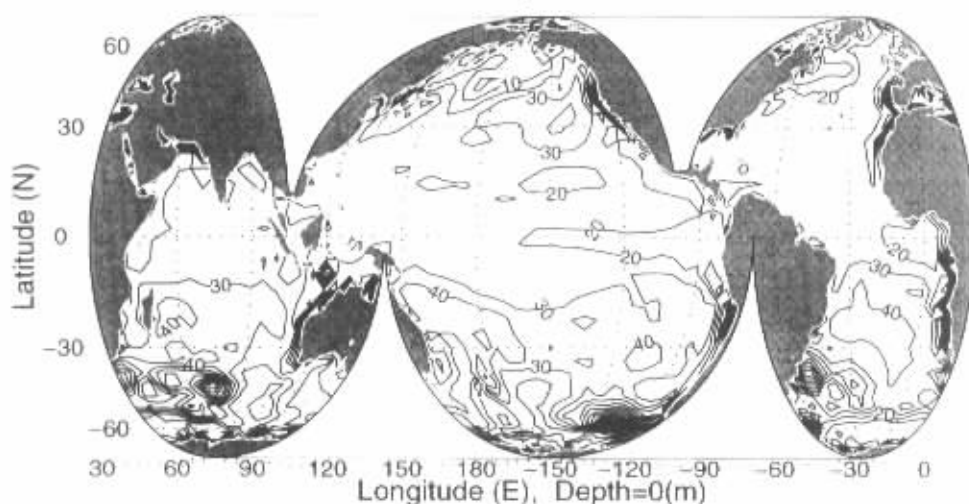

SH flux monthly mean Jul 1978

Fig. 5. Monthly mean surface sensible heat flux (W / m^2) simulated by the GISS Coupled Model:
(a) January 1978, and (b) July 1978.

(1978) upward sensible heat flux at the ocean surface (Q_H), respectively. Large values of Q_H can be expected in air which is very much cooler than the surface of the ocean across which it is flowing, especially when the wind is strong. Therefore, it is not surprising to find large values of Q_H occur over the Gulf Stream and Kuroshio Systems, the Bering Sea, the Arctic Ocean during northern winter (Fig. 5a) and over the southern ocean near Antarctic (Fig. 5b) since at that time of year prevailing winds advect cold air over the water from neighboring
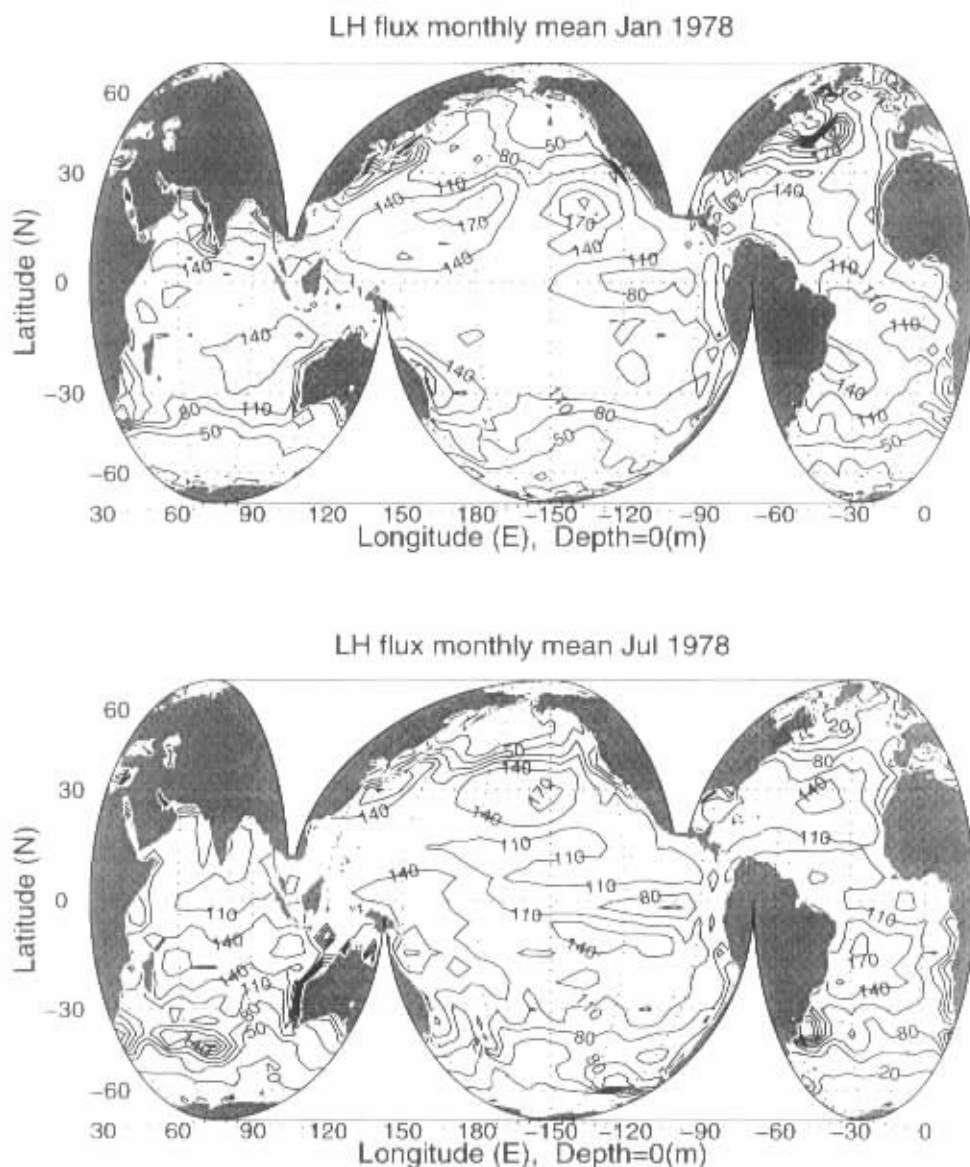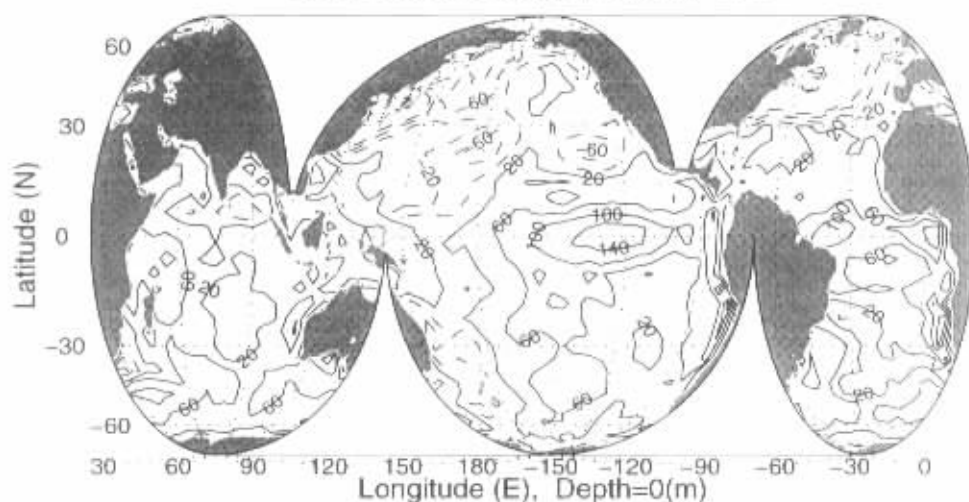
LH flux monthly mean Jan 1978

LH flux monthly mean Jul 1978

Fig. 6. Monthly mean surface latent heat flux (W / m²) simulated by the GISS Coupled Model: (a) January 1978, and (b) July 1978.

land masses or ice–sheets.

Latent heat flux

Figures 6a and 6b show the GISS coupled model output of mean January and July (1978) upward sensible heat flux at the ocean surface (Q_E), respectively. We may find the same features as obtained from earlier studies such as Budyko (1956): (a) The values of Q_E are almost everywhere greater in winter than in summer. (b) The high values of Q_E are found

Net heat flux monthly mean Jan 1978

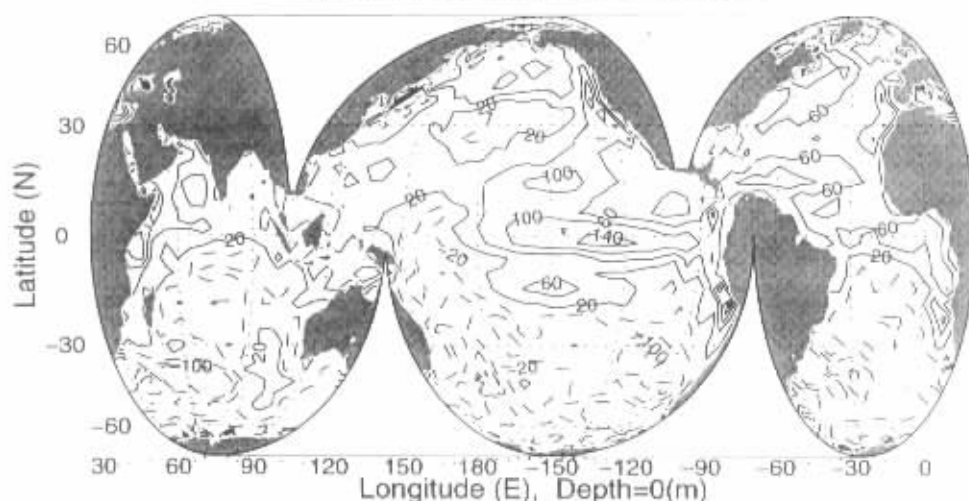## Net heat flux monthly mean Jul 1978

Fig. 7. Monthly mean surface net downward heat flux (W/m^2) simulated by the GISS Coupled Model: (a) January 1978, and (b) July 1978.

near the western boundaries of the North Atlantic and North Pacific Oceans in northern winter (Fig. 6a). (c) Seasonal variations of Q_E are nowhere greater than over the Gulf Stream and Kuroshio Systems. (d) Over the eastern parts of oceans seasonal variations are very much smaller, because at all times of the year prevailing winds advect maritime air (moist) over the cool ocean. (e) Throughout the year high values of Q_E ($\geqslant 170 \ W/m^2$) occur in the subtropics and in trade—wind belts.

Downward net surface heat flux

After examining temporal and spatial variations of each component of the surface energy budget, we computed the net downward surface heat flux using Eq. (1). Figures 7a and 7b show the GISS coupled model output of mean January and July (1978) downward net heat flux at the ocean surface (Q), respectively. It has strong seasonal variation: positive values in summer hemisphere and negative values (upward flux) in winter hemisphere. Furthermore, strong net heat flux occurs in equatorial regions with a maximum value of 140 W / m^2.

3. Statistical evaluation

3.1 *Cross—correlation coefficient*

Same as in Chu et al. (1998), the validity of Haney—type boundary conditions (3), and (5) should be first tested by cross—correlation coefficients (CCC) between the two time series: Q[or $\tilde{Q}$] and ΔT at day d, which is computed in this paper from a 91—day subset between 45 days prior to and 45 days after that date,

$$R_{Q,\Delta T}(d)= \frac{\frac{1}{N}\sum_{i=1}^{N}\{[Q(x,y,\tau_i)- \overline{Q}(x,y)][\Delta T(x,y,\tau_i)- \overline{\Delta T}(x,y)]\}}{\sigma_Q(d)\sigma_{\Delta T}(d)}$$

$$(d- 45\leqslant \tau_i \leqslant d+ 45) \tag{6}$$

where $N= 91$ (day), (x,y) the horizontal coordinates, $\overline{Q}(x,y)$ and $\overline{\Delta T}(x,y)$ the temporal means of the subset data, and $\sigma_Q(d)$ and $\sigma_{\Delta T}(d)$ the standard deviations of the subset data.

Thus, we established little over one year (368 days, 17 March 1978—20 March 1979) CCC data sets: $R_{Q,\Delta T}$, and $R_{\tilde{Q},\Delta T}$. The higher the values of CCC, the higher the confidence of linear relationship between $(Q,\tilde{Q})$ and ΔT.

Besides the correlation analysis, we need to do the variance analysis, because it does matter if $(Q,\tilde{Q})$ and ΔT correlate wonderfully, but typically used values of κ end up missing all the variance.

3.2 *Statistical tests*

Whether the sample values of $R_{Q,\Delta T}$ represent good or bad linear relationships (3), and (5) between $(Q,\tilde{Q})$ and ΔT should be tested. First, we use the t—test

$$t= \frac{R_{Q,\Delta T}\sqrt{N- 2}}{\sqrt{1- R_{Q,\Delta T}}} \quad , \tag{7}$$

to identify the region with small values of CCC in which there is no correlation between $(Q,\tilde{Q})$ and ΔT. We begin with the null hypothesis that the two variables Q and ΔT are not positively correlated. The significance level α is the probability that the given value of t is exceeded purely by chance. Equivalently, it is the probability of incorrectly rejecting the null hypothesis. For a given significance level $\alpha(\alpha= 0.05$ was used), we compare the t—value with t_α, if $t< t_\alpha$, we accept the null hypothesis, and there is no linear (positive) relationship between Q and ΔT at the given location (x,y).

Second, we set up a prior significant value (ρ_0) for CCC, and use the z—test

$$z = \frac{\sqrt{N-3}}{2} \ln\left[\frac{(1+R_{Q,\Delta T})(1-\rho_0)}{(1-R_{Q,\Delta T})(1+\rho_0)}\right] , \tag{8}$$

to see if CCC is significantly larger than ρ_0. This z−value is satisfying the normal distribution.

We start with the null hypothesis that $H_0 : R_{Q,\Delta T} = \rho_0, H_1 : R_{Q,\Delta T} > \rho_0$. The significance level α is the probability that the given value of z is exceeded purely by chance. For a given significance level $\alpha(\alpha = 0.05$ was used), we compare the z−value with z_α, if $z > z_\alpha$, we accept H_1, and the CCC between Q and ΔT exceeds ρ_0 at the given location (x,y). In this study, we use $\rho_0 = 0.7$.

4. CCC fields over the world oceans

The time series $R_{Q,\Delta T}(x,y,d)$, and $R_{\tilde{Q},\Delta T}(x,y,d)$ were decomposed into ensemble means

$$\langle R_{Q,\Delta T} \rangle = \frac{1}{368}\sum_d R_{Q,\Delta T}(x,y,d) \ ,\langle R_{\tilde{Q},\Delta T} \rangle = \frac{1}{368}\sum_d R_{\tilde{Q},\Delta T}(x,y,d) \ , \tag{9}$$

which show the overall linear relationships between $(Q,\tilde{Q})$ and ΔT and anomalies

$$R'_{Q,\Delta T} = R_{Q,\Delta T} - \langle R_{Q,\Delta T} \rangle \ ,R'_{\tilde{Q},\Delta T} = R_{\tilde{Q},\Delta T} - \langle R_{\tilde{Q},\Delta T} \rangle \ , \tag{10}$$

which indicate temporal variations of such relationships. The region with large CCC values $(\geqslant 0.7)$ is called the valid region, and the region with small CCC absolute values $(\leqslant 0.2)$ is called the invalid region.

4.1 Ensemble mean CCC fields

The ensemble means $\langle R_{Q,\Delta T} \rangle$ (Fig. 8a) and $\langle R_{\tilde{Q},\Delta T} \rangle$ (Fig. 8b) have a strong latitudinal variation: very small absolute values in the equatorial zone (10°S−10°N), and quite large values in the middle and high latitudes. These features are very similar to the analysis on the NCEP re−analyzed surface data (Chu et al., 1998). However, $\langle R_{Q,\Delta T} \rangle$ and $\langle R_{\tilde{Q},\Delta T} \rangle$ are quite different in the middle and high latitudes. The values of $\langle R_{Q,\Delta T} \rangle$ are less than 0.7 almost everywhere except in small regions of the South Atlantic Ocean and the western Indian Ocean between 30°S and 50°S, which is generally lower than the analysis on the NCEP data (Chu et al., 1998). On the other hand, the values of $\langle R_{\tilde{Q},\Delta T} \rangle$ are greater than 0.8, which is generally higher than the analysis on the NCEP data (Chu et al., 1998). Therefore according to the GISS coupled model results, the Haney−type boundary condition without solar radiation is a good representation in the middle and high latitudes (higher than 30°S). The invalidity in the equatorial regions (10°S−10°N) may imply the improper representation of latent heat flux Q_E by temperature difference ΔT. To confirm this, we computed CCC between latent heat flux Q_E and $- \Delta T$ (Fig. 9). The world oceans are therefore divided into two parts: (a) equatorial zone with no correlation between Q_E and $- \Delta T$, and (b) mid− and high− latitude zones with evident correlation $(\geqslant 0.5)$.

4.2 Anomaly CCC fields

We used Empirical Orthogonal Function (EOF) analysis to delineate the major modes of variability of the anomaly CCC field: $R'_{Q,\Delta T}$, which is decomposed by

$$R' = \sum_\alpha PC_\alpha(d)\varphi_\alpha(x_i,y_j) \tag{11}$$

with solar radiation

(a)

Longitude (E), Depth=0(m)

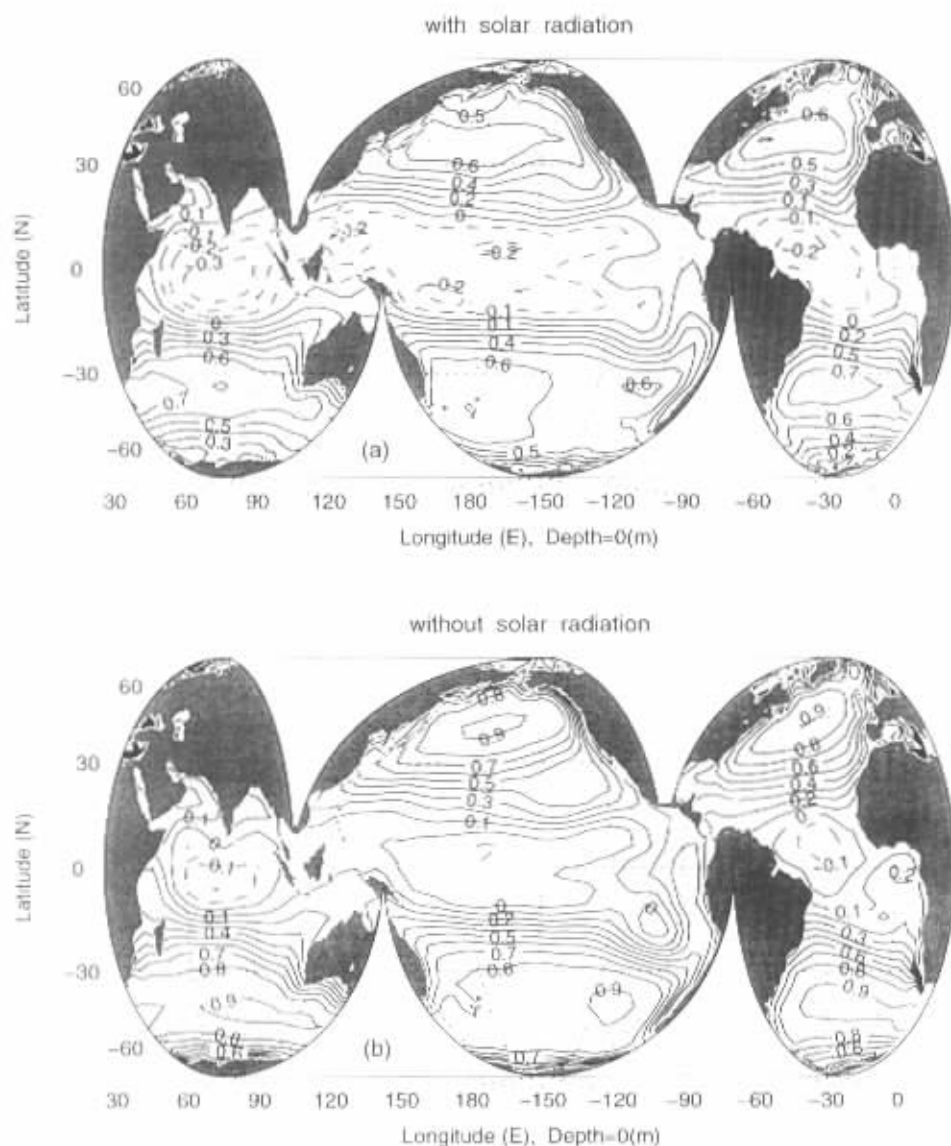without solar radiation

(b)

Longitude (E), Depth=0(m)

Fig. 8. Annual mean cross–correlation coefficients between ΔT and net surface heat flux: (a) with solar radiation Q, and (b) without solar radiation $\tilde{Q}$.

where $PC_s(d)$ is the principal component, representing the temporal variation of the associated spatial pattern described by EOF $\varphi_s(x_i, y_i)$. The time series is analogous to a projection of CCC anomaly through the ' filter' of an EOF mode during a time scale.

The first leading EOF is able to account for 67% (71%) of the total variance with (without) solar radiation during the integration period (Table 1.) Each EOF mode is normalized so that its spatial variance is equal to unity. So, those patterns of the first EOF are enough to explain the spatial anomalies of the global CCCs. Here, we only show EOF1 and PC_1 as an example.
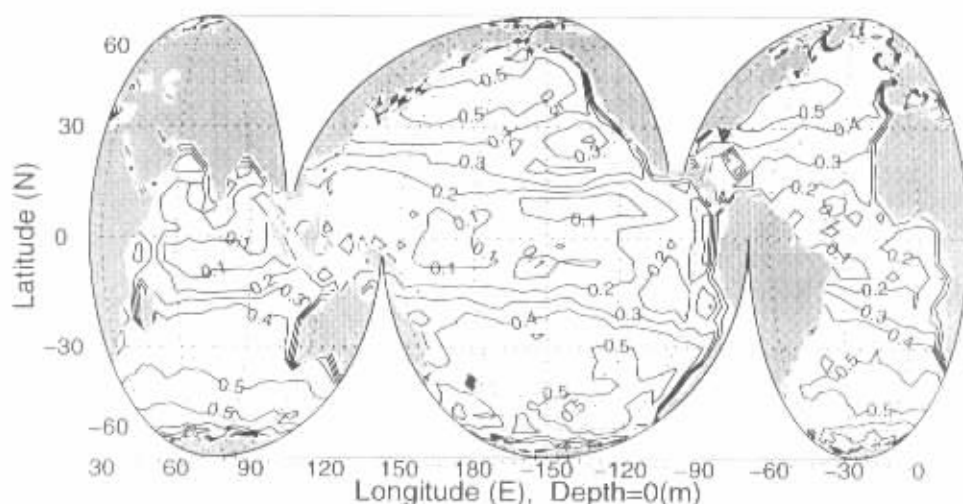
CCC To–Ta and Latent Heat Flux

Fig. 9. Annual mean cross–correlation coefficients between $-\Delta T$ and latent heat flux.

Table 1. Variances of the first six leading EOFs for the gradient–type conditions

EOF	With Solar Radiation	Without Solar Radiation
1	0.670	0.712
2	0.189	0.139
3	0.073	0.056
4	0.020	0.025
5	0.014	0.020
6	0.009	0.012

EOF1 mode (Fig. 10a) has a dipole pattern featuring the Northern Hemisphere positive (maximum value near 0.04) and Southern Hemisphere negative (minimum value near -0.04), and accounts for up to 67% of the total spatial variance. This pattern is believed to be related to the solar radiation. The first principal component, $PC_1(d)$, during the integration period is shown in Fig. 10b. EOF1 mode $\varphi_1(x_i, y_i)$, is generally positive (negative) in the Northern (Southern) Hemisphere (Fig. 10a). Therefore, $PC_1(d) > 0$, corresponds to positive (negative) CCC anomalies in the Northern (Southern) Hemisphere, and $PC_1(d) < 0$, corresponds to negative (positive) CCC anomalies in the Northern (Southern) Hemisphere. From early October when $PC_1(d) = 0$, it increases with time until the end of December when PC_1 reaches the maximum value of 10.0, and then decreases to 0 in late March. After late March, PC_1 becomes negative until early October and reaches the minimum value of -10.0 in early July. From early October to early March, the Northern (Southern) Hemisphere is winter (summer), $PC_1(d) > 0$. The contribution of EOF1 to the total CCC field, $PC_1(d) \times \varphi_1(x_i, y_i)$, adds positive values to the ensemble CCCs with a maximum increasing value of $0.4[= 10.0 \times 0.04]$ in the Northern Hemisphere and adds negative values to the ensemble CCCs with a maximum
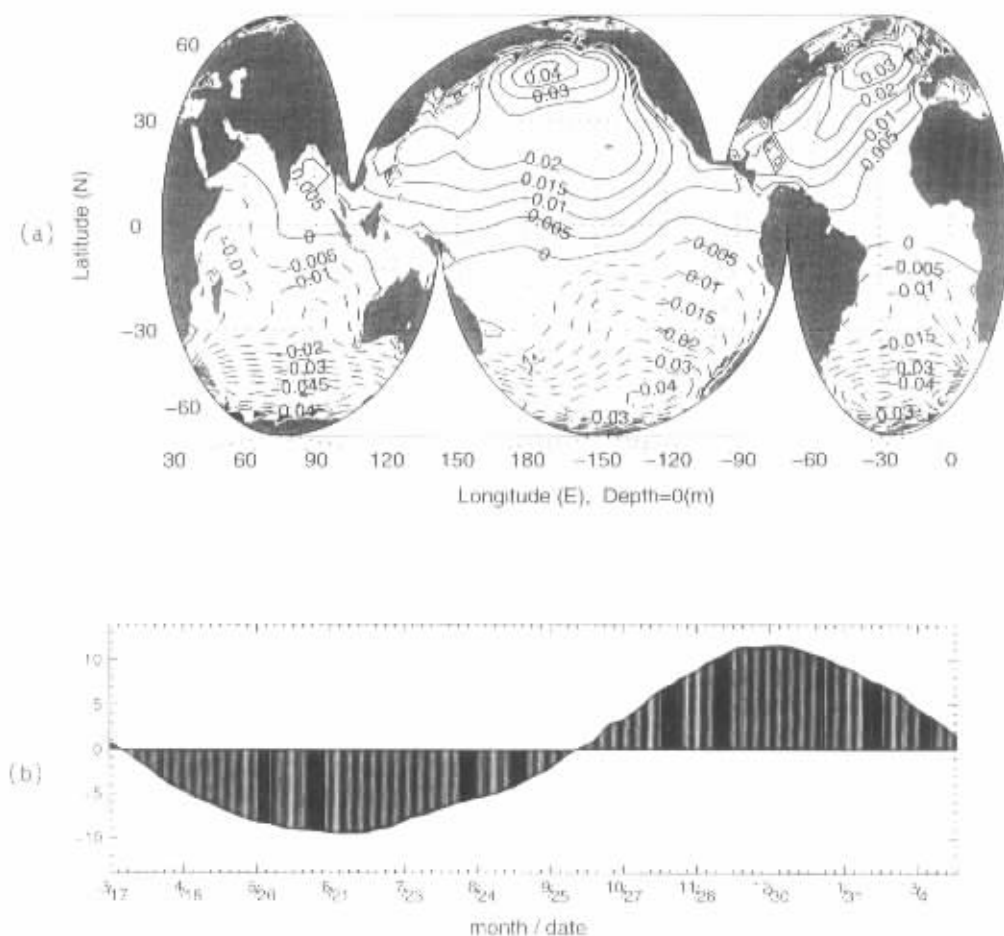
Fig. 10. (a) First EOF mode of $R'_{2,\Delta r}$, and (b) associated time series of PC_1.

decreasing value of $-0.4[= 10.0 \times (-0.04)]$ in the Southern Hemisphere. On the other hand, from early March to early October, $PC_1(d) < 0$. The contribution of EOF1 to the total CCC field is reversed to the period from early October to early March. Thus, the winter hemisphere has better cross-correlations than the summer hemisphere. The maximum temporal variability can reach 0.8 ($= 2 \times 0.4$). Thus, the Haney-type thermal boundary condition with solar radiation is valid only in the winter.

The physical interpretation to the results that the winter hemisphere has better cross-correlation between heat flux and air–sea temperature difference than the summer hemisphere is that the values of R_S are almost everywhere smaller in winter than in summer, and R_S cannot be parameterized by the air–sea temperature difference.

5. Seasonal CCC variation in five geographic zones

On the basis of the spatial variation of the ensemble mean field, we divided the world oceans into five geographic zones: equatorial zone ($10°N–10°S$), northern subtropical zone
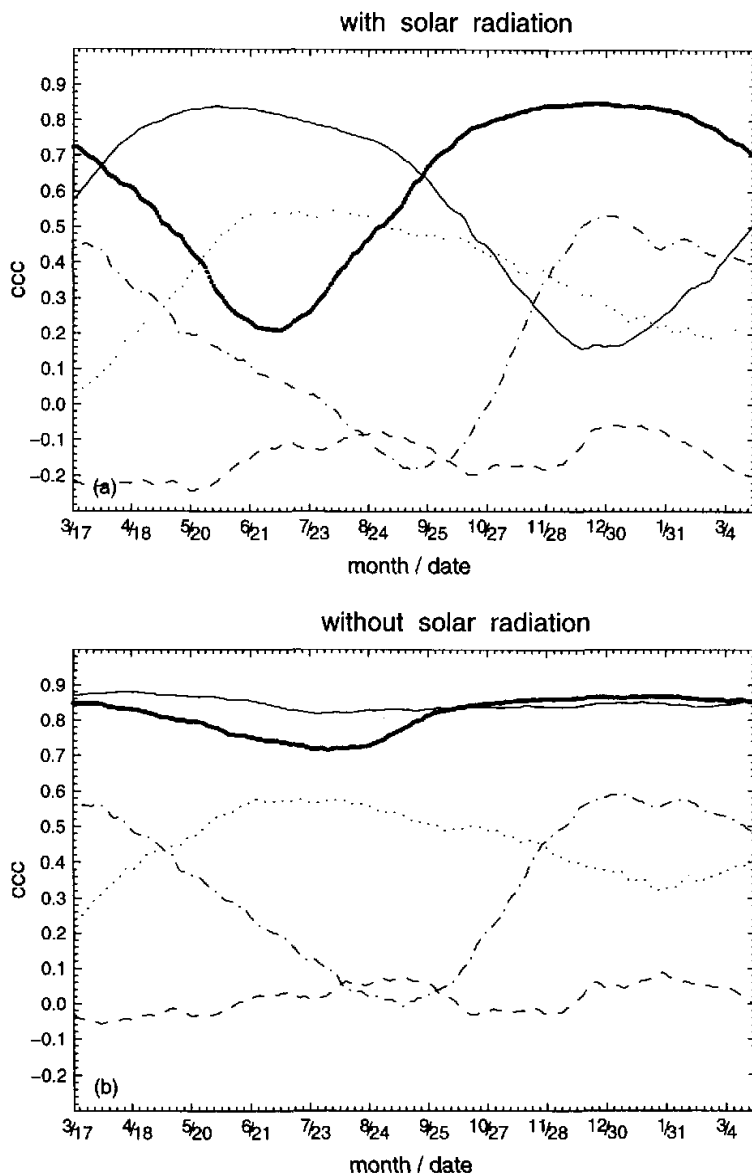
with solar radiation

(a)

month / date

without solar radiation

(b)

month / date

Fig. 11. Seasonal variation of cross–correlation coefficients averaged within five geographic zones between (a) Q and ΔT, and (b) $\bar{Q}$ and ΔT. Here, the thin solid curve indicates the southern middle and high latitude zone (south to 30°S), the thick solid curve indicates the northern middle and high latitude zone (north to 30°N), the dotted curve indicates the southern subtropical zone (10–30°S), the dashed–dotted curve indicates the northern subtropical zone (10–30°N), and the dashed curve indicates the equatorial zone (10°S–10°N).

$(10-30°N)$, southern subtropical zone $(10-30°S)$, northern middle and high latitude zone (north to $30°N$), and southern middle and high latitude zone (south to $30°S$). At each day, we averaged the CCC data $R_{Q,\Delta T}(x,y,d)$, and $R_{\tilde{Q},\Delta T}(x,y,d)$ spatially within each zone. Thus, we obtained five time series for each of the CCC data: $\overline{R}^S_{Q,\Delta T}(d), \overline{R}^S_{\tilde{Q},\Delta T}(d)$. Here, the superscript 'S' means the spatial average.

5.1 *With solar radiation*

The seasonal variation of $\overline{R}^S_{Q,\Delta T}(d)$ for the five geographic zones (Fig. 11a) is much stronger than that for the NCEP data (Chu et al., 1998). The value of $\overline{R}^S_{Q,\Delta T}(d)$ fluctuates from -0.25 to -0.08 in the equatorial zone (no correlation between Q and ΔT), from 0.04 to 0.54 in the southern subtropical zone, and from -0.2 to 0.5 in the northern subtropical zone (weak correlation between Q and ΔT). However, the cross-correlation coefficient $\overline{R}^S_{Q,\Delta T}(d)$ has a seasonal variation (0.2 to 0.86) in both the northern and southern middle and high latitude zones with $180°$ phase shift: higher values during winter and lower values during summer. Such a feature (winter hemisphere has a higher correlation) is due to small values of solar radiation (R_S) in winter hemisphere. Among the four components in the net surface heat flux (Q), only solar radiation cannot be represented the air-sea temperature difference ΔT.

The period when $\overline{R}^S_{Q,\Delta T}(d) > 0.7$ (valid period) is from 25 September to 15 March in the northern middle and high latitudes and from 30 March to 1 September in the southern middle and high latitudes. Such a strong seasonal variation of $\overline{R}^S_{Q,\Delta T}(d)$ in the middle and high latitudes indicates the improper representation of the solar radiation R_S by the temperature difference ΔT.

5.2 *Without solar radiation*

Figure 11b illustrates the seasonal variation of $\overline{R}^S_{\tilde{Q},\Delta T}(d)$ for the five geographic zones. The correlation is higher between $\tilde{Q}$ and ΔT than between Q and ΔT, indicating the benefit of excluding the solar radiation from the net surface heat flux. For example, $\overline{R}^S_{\tilde{Q},\Delta T}(d)$ is near 0.86 all year round in the southern middle and high latitudes, and varies between 0.74 and 0.88 in the northern middle and high latitudes. However, $\overline{R}^S_{\tilde{Q},\Delta T}(d)$ is still very low (between -0.06 and 0.06) in the equatorial zone, and becomes higher but less than 0.7 in both northern and southern subtropical zones.

6. Seasonal variation of relaxation coefficient κ

Since the value of κ is quite uncertain, such a variance comparison between $(Q,\tilde{Q})$ and ΔT depends on the choice of κ. If κ is determined by

$$\kappa(d) = \frac{\sigma_Q(d)}{\sigma_{\Delta T}(d)} R_{Q,\Delta T} \tag{12}$$

at each time instance d, the variance of Q equals the variance of $\kappa\Delta T$. This is so-called no-missing variance to estimate Q by $\kappa\Delta T$. Now, we should check if values of κ calculated by (12) are within the reasonable range.

with solar radiation
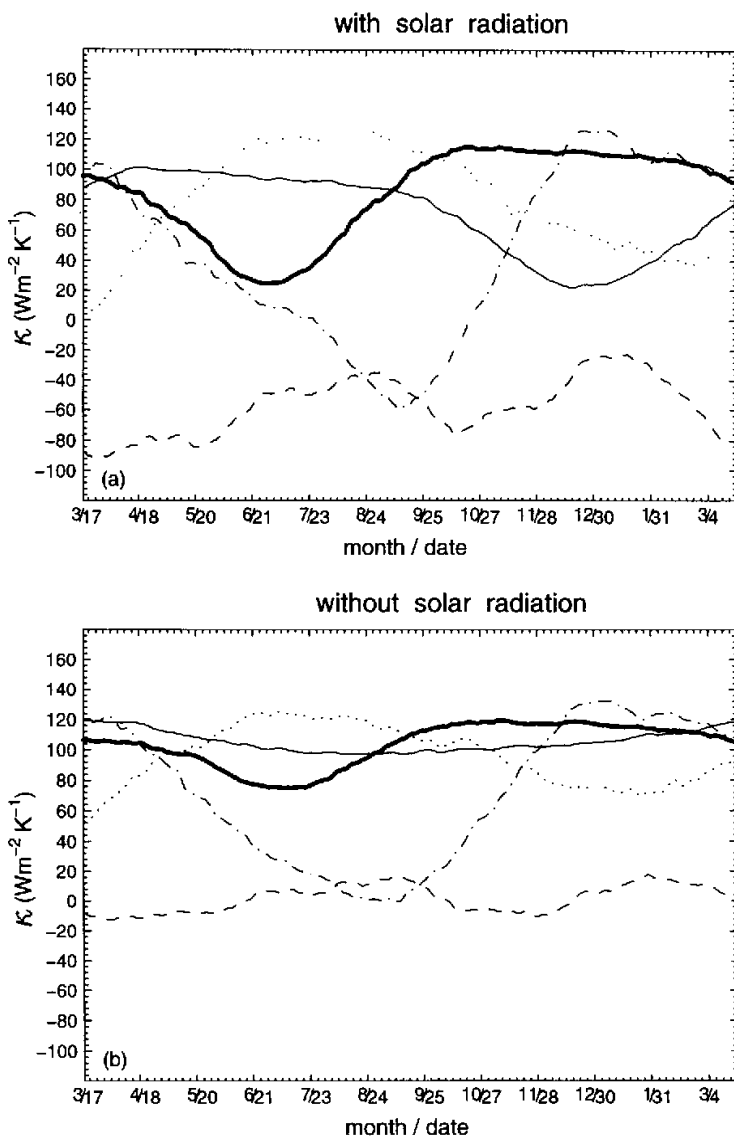

(a)

without solar radiation

(b)

Fig. 12. Seasonal variation of relaxation coefficient κ averaged within five geographic zones, determined by no loss of variance for (a) $Q = \kappa\Delta T$, and (b) $\tilde{Q} = \kappa\Delta T$. Here, the thin solid curve indicates the southern middle and high latitude zone (south to 30°N), the thick solid curve indicates the northern middle and high latitude zone (north to 30°S), the dotted curve indicates the southern subtropical zone (10–30°S), the dashed–dotted curve indicates the northern subtropical zone (10–30°N), and the dashed curve indicates the equatorial zone (10°S–10°N).

We computed the relaxation coefficient κ using (12) and then averaged κ spatially within each of the five zones. Thus, we obtained both the spatial (five zones) and the temporal variability of κ. Theoretically, κ can be time–dependent. Practically, κ is usually taken as a constant in the surface thermal boundary conditions (3), and (5). Therefore besides high cross correlations, we should also consider quasi–steadiness of κ in evaluating the surface thermal boundary conditions.

For surface net heat flux with solar radiation (Fig. 12a), κ varies from -90 to -20 $Wm^{-2}K^{-1}$ in the equatorial zone, from 0 to 130 $Wm^{-2}K^{-1}$ in the southern subtropical zone, from -20 to 124 $Wm^{-2}K^{-1}$ in the northern subtropical zone, from 20 to 100 $Wm^{-2}K^{-1}$ in the southern middle and high latitude zone, and from 20 to 120 $Wm^{-2}K^{-1}$ in the northern middle and high latitude zone. When the solar radiation is excluded from the net surface heat flux (Fig. 12b), κ has small temporal variations in all the five geographic zones. For example, κ varies from 80 to 120 $Wm^{-2}K^{-1}$ in the northern middle and high latitudes and from 100 to 120 $Wm^{-2}K^{-1}$ in the southern middle and high latitudes.

On the basis of (a) high correlation between $\tilde{Q}$ and ΔT_1, and (b) quasi–steadiness of κ, we may conclude that the surface thermal boundary condition

$$\tilde{Q} = \kappa \Delta T$$

is a good parameterization of surface net heat flux for the middle and high latitudes.

7. Variance analysis for the haney–type condition

The coupling coefficient κ has units of watts per square meter per kelvin. A time–scale can be derived as $\tau = \rho c_p h / \kappa$, where ρ is the density, c_p is the specific heat of seawater, and h is a typical mixed layer depth. Weaver and Sarachik (1991) used a time–scale of 25 days. Marotzke and Stone (1995) used 30 days. For a mixed layer 50 m deep these correspond to values of κ of 97 $Wm^{-2}K^{-1}$ and 81 $Wm^{-2}K^{-1}$, respectively. As pointed by a number or authors (Rahmstorf and Willibrand, 1995; Pierce et al., 1995; Cai and Chu 1996), change of values of κ has detrimental effects on the realism of a modeled thermohaline circulation. Thus, use of a proper κ–value becomes an important issue.

We computed the standard deviations of $\tilde{Q}$, and $\kappa \Delta T$ averaged over the northern and southern middle and high latitude zones: $\sigma_Q(d)$ and $\sigma_{\kappa\Delta T}(d)$. The relaxation coefficient κ has values of 30, 60, 90, and 120 $Wm^{-2}K^{-1}$. For a given day, d, the standard deviation $\sigma_{\kappa\Delta T}(d)$ increases with κ. When $\kappa = 120$ $Wm^{-2}K^{-1}$, the two standard deviations, $\sigma_{\tilde{Q}}(d)$, and $\sigma_{\kappa\Delta T}(d)$, are quite close in both northern (Fig. 13a) and southern (Fig. 13b) middle and high latitude zones. The large value of κ (120 $Wm^{-2}K^{-1}$) might be caused by a short coupling time–scale, since in the GISS coupled model atmospheric and oceanic surface fluxes of water, heat (excluding solar radiation), and momentum are of opposite sign and are applied synchronously.

8. Conclusions

On the basis of cross–correlation and variance analyses, we obtain the following results:

(1) The Haney–type conditions, $Q = \kappa \Delta T$ and $\tilde{Q} = \kappa \Delta T$, have better representation of surface heat forcing in the middle and high latitudes than in the equatorial regions. On the basis of high correlation between $\tilde{Q}$ and ΔT and associating quasi–steadiness of κ,
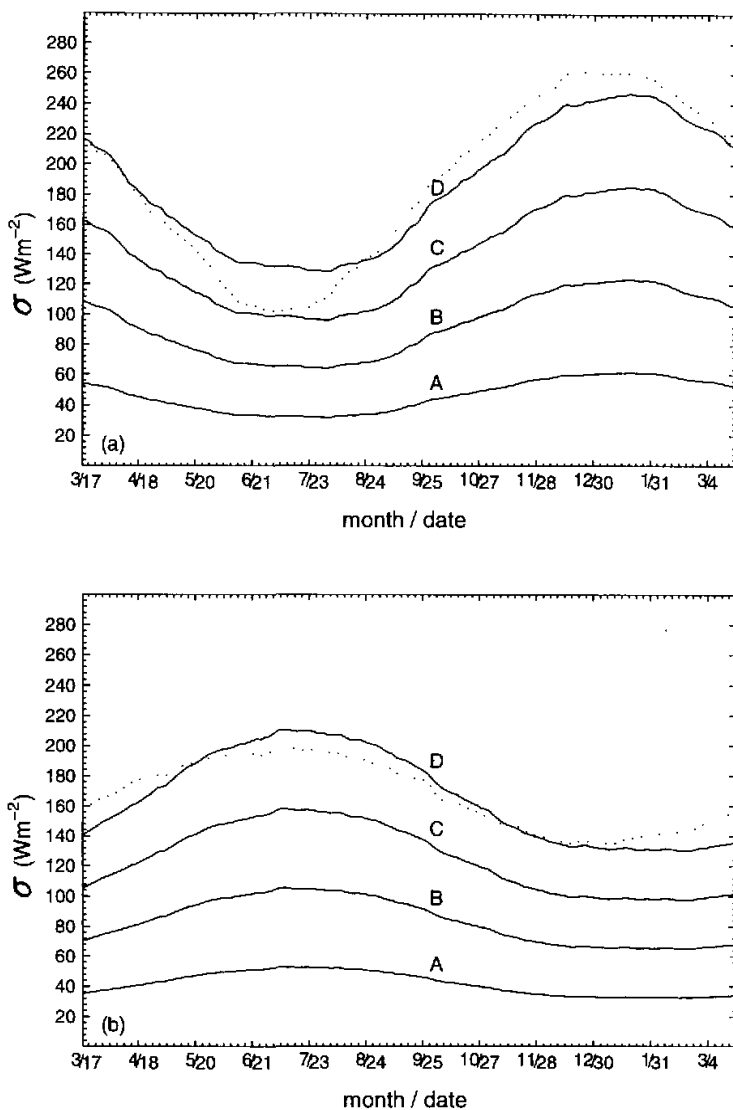
Fig. 13. Comparison among $\sigma_{\dot{Q}}$ (dashed curve), and $\sigma_{\kappa\Delta T}$ at different values of κ(A:$\kappa = 30$ Wm^{-2}K^{-1}, B: $\kappa = 60$ Wm^{-2}K^{-1}, C: $\kappa = 90$ Wm^{-2}K^{-1}, and D: $\kappa = 120$ Wm^{-2}K^{-1}) for (a) northern middle and high latitudes, and (b) southern middle and high latitudes.

we recommend to use $\tilde{Q} = \kappa \Delta T$ for the middle and high latitude surface thermal forcing.

(2) For the equatorial and subtropical oceans, the Haney–type conditions, $Q = \kappa \Delta T$ and $\tilde{Q} = \kappa \Delta T$, are not good approximations for the surface thermal forcing.

(3) A value of 120 $Wm^{-2}K^{-1}$ for the relaxation coefficient κ is suggested. When κ is taken as 120 $Wm^{-2}K^{-1}$, the variance of surface net heat flux $\tilde{Q}$ can be well represented by the variance of $\kappa \Delta T$. This value is much higher than that estimated from the NCEP data.

(4) Quantitative values of correlation coefficient and relaxation coefficient may vary with the eddy viscosity and diffusivity. But the results on validity of the Haney–type boundary condition holds.

REFERENCES

Blumberg, A., and G. Mellor, 1987: A description of a three dimensional coastal ocean circulation model. In: *Three Dimensional Coastal Ocean Models* (edited by N.S. Heaps), American Geophysical Union, Washington D. C., 1–16.

Budyko, M. I., 1956: teplovoi balans zemnoi poverkhnosti, Gidrometeorologicheskoe izdatelstvo, Leningrad, 255 pp (US Weather Bureau translation: 'Heat balance at the earth surface', 1958, PB131692, 259 pp).

Cai, W. J., and P. C. Chu, 1996: Ocean climate drift and interdecadal oscillation due to a change in thermal damping. *J. Climate,* **9**, 2821–2833.

Chu, P. C., Y. C. Chen, and S. H. Lu, 1998: On Haney–type surface thermal boundary conditions for ocean circulation models. *J. Phys. Oceanogr.,* **28**, 890–901.

Greatbatch, R. J., G. Li, and S. Zhang, 1995: Hindcasting ocean climate variability using time–dependent surface data to drive a model: An idealized study. *J. Phys. Oceanogr.,* **25**, 2715–2725.

Han, Y. J., 1984: A numerical world ocean general circulation model. Part II: A baroclinic experiment. *Dyn. Atmos. Oceans,* **8**, 141–172.

Haney, R. L., 1971: Surface thermal boundary condition for ocean circulation models. *J. Phys. Oceanogr.,* **1**, 241–248.

Hansen, J., G. L. Russell, D. Rind, P. Stone, A. Lacis, S. Lebedef, R. Ruedy, and L. Travis, 1983: Efficient three–dimensional global models for climatic studies: Models I and II. *Mon. Wea. Rev.,* **111**, 609–662.

Kleeman, R., and S. B. Power, 1995: A simple atmospheric model of surface heat flux for use in ocean modeling studies. *J. Phys. Oceanogr.,* **25**, 92–105.

Marotzke, J., and P. Stone, 1995: Atmospheric transports, the thermohaline circulation, and flux adjustments in a simple coupled model. *J. Phys. Oceanogr.,* **25**, 1350–1364.

Oberhuber, J. M., 1988: An atlas based on the COADS data set: The budgets of heat, buoyancy and turbulent kinetic energy at the surface of the global ocean. *Tech. Rep.,* **15**, Max–Planck Institut fur Meteorologie, 199 pp.

Pierce, D., T. P. Barnett, and U. Mikolajewicz, 1995: Competing roles of heat and freshwater flux in forcing thermohaline oscillations. *J. Phys. Oceanogr.,* **25**, 2046–2064.

Rahmstorf, S., and J. Willebrand, 1995: The role of temperature feedback stabilizing the thermohaline circulation. *J. Phys. Oceanogr.,* **25**, 787–805.

Russell, G. L., J. R. Miller, and D. Rind, 1995: A coupled atmosphere–ocean model for transient climate change studies. *Atmosphere–Ocean* **33**, 683–730.

Shapiro, R., 1970: Smoothing filtering and boundary effects. *Rev. Geophys. Space Phys.,* **8**, 359–387.

Weaver, A. J., and E. S. Sarachik, 1991: Evidence for decadal variability in an ocean general circulation model: An advective mechanism. *Atmos. –Ocean,* **29**, 197–231.

Xu, W., R. J. Greatbatch, and C. A. Lin, 1995: The sensitivity of an eddy–resolving model to the surface thermal boundary conditions. *J. Geophys. Res.,* **100**, 15899–15914.